Supplementary Information

All-nanofiber–based, ultrasensitive, gas-permeable mechanoacoustic sensors for continuous long-term heart monitoring

Md Osman Goni Nayeem[a], Sunghoon Lee[a], Hanbit Jin[a], Naoji Matsuhisa[a], Hiroaki Jinno[a,b], Akihito Miyamoto[a], Tomoyuki Yokota[a], and Takao Someya[a,b,c*]

[a] Department of Electrical Engineering and Information Systems, School of Engineering, The University of Tokyo, 7-3-1 Hongo, Bunkyo-ku, Tokyo 113-8656, Japan

[b] Center for Emergent Matter Science (CEMS), RIKEN, 2-1 Hirosawa, Wako, Saitama 351-0198, Japan

[c] Thin-Film Device Laboratory, RIKEN, 2-1 Hirosawa, Wako, Saitama 351-0198, Japan

* All correspondence should be sent to someya@ee.t.u-tokyo.ac.jp.

This supplementary information contains:

Supplementary Notes, Supplementary Figures S1-S16, Supplementary Table S1, List of Supplementary Movies (S1 and S2), and Supplementary References (1-2).

www.pnas.org/cgi/doi/10.1073/pnas.1920911117

Supplementary Notes:

Reason of using PU with coated metal layer as electrodes:

For on skin sensors, softness is required along with the conductivity. Therefore, we have chosen soft polymer (PU) nanofibers with 100-nm-thick Au layer. PU nanofibers sheet exhibits sufficiently low effective Young's modulus of 0.274 ± 0.039 MPa (ref 44 in the manuscript), compared to that of plasticized carbon fibers sheet (0.2–0.8 GPa, ref 1 in SI). Furthermore, the conductivity of 100 nm thick Au layer on PU nanofibers is sufficiently high (sheet resistance, 2.293 ± 0.069 Ω) to generate piezo-/triboelectricity signals.

Effect of electrode coverage area

To quantify the covered area by PU nanofiber, we have analyzed the SEM image (Figure S6). Maximum coverage area is plotted as a function of electrospinning time. We have used low density PU nanofiber layer coated by Au (max. coverage area 39.07%) as electrode layers.

For triboelectric sensors, higher contact area can increase the charge generation. On the other hand, higher opening area decreases the air damping effect which enables the larger vibration of the sensors (ref 2 in SI, ref 29 in the manuscript). These effects are in trade-off. In this time, we optimized the density of PU nanofiber layer, and used low density PU nanofiber layer coated by Au (max. coverage area 39.07%) as electrode layers to achieve the highest signals.

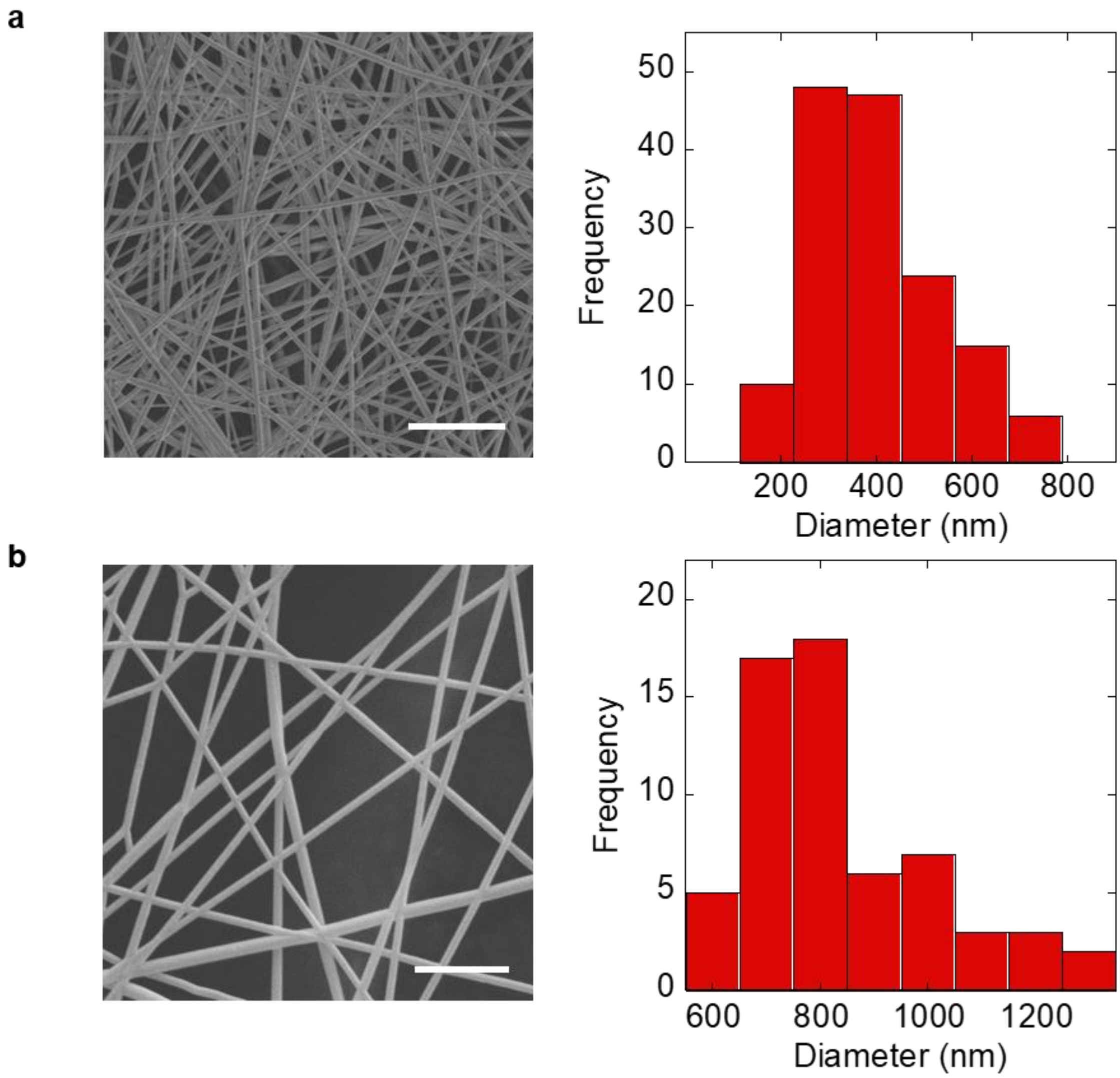

Figure S1

SEM image of electrospun nanofibers, and diameter distribution a, PVDF nanofiber (e-spinning condition: 19 wt%, 20 kV and 10 μL/min). **b,** Parylene coated PU nanofiber (e-spinning condition: 15 wt%, 20 kV and 10 μL/min). Scale bar, 10 μm.

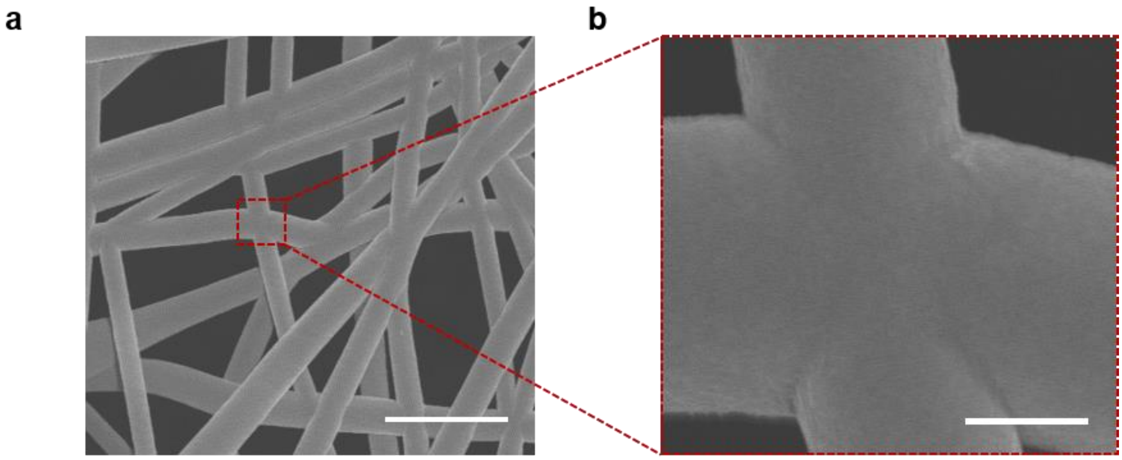

Figure S2

Surface SEM image of **a,** parylene coated PU nanofiber. Scale bar, 5 µm. **b,** 10x magnified image showing stronger fiber–to–fiber joint due to thin layer of parylene coating. Scale bar, 500 nm.

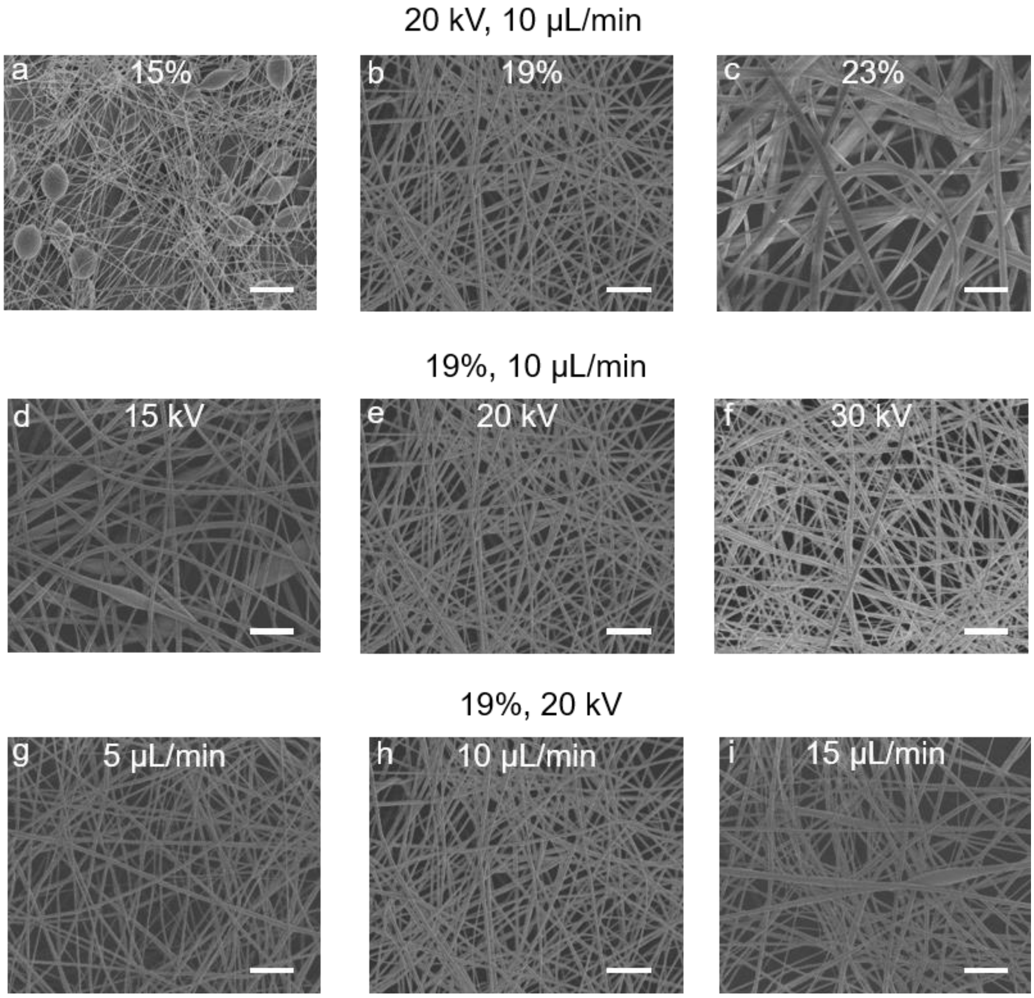

Figure S3

Surface SEM images of PVDF nanofibers at various electrospinning conditions. PVDF nanofiber fabrication conditions were optimized by varying electrospinning conditions. a-c, Variation of solution concentration (20 kV, 10 μL/min) **d-f,** Variation of applied voltage (19wt%, 10 μL/min) and **g-i,** Variation of pumping rate (19 wt%, 20 kV). Scale bar, 10 μm.

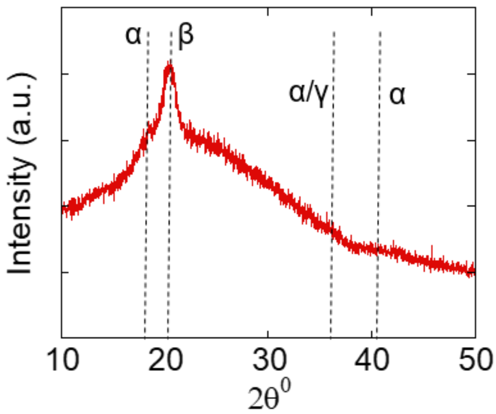

Figure S4

XRD pattern of PVDF nanofibers. Peak at 2θ ≈ 20.2°, which corresponds to diffraction in (110) plane and represents the β-phase formation.

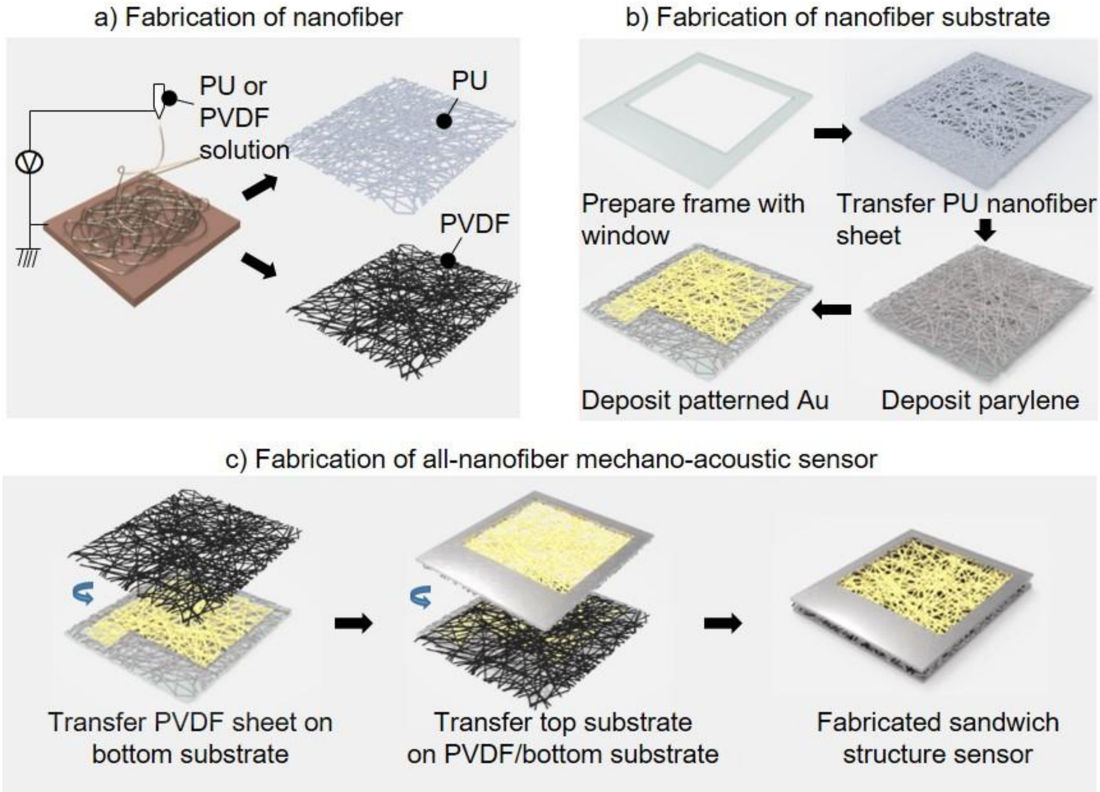

Figure S5

Schematic illustration of device fabrication process. a, Fabrication of nanofiber using electrospinning method **b,** Fabrication of nanofiber substrate **c,** Fabrication of final sensor by transfer method.

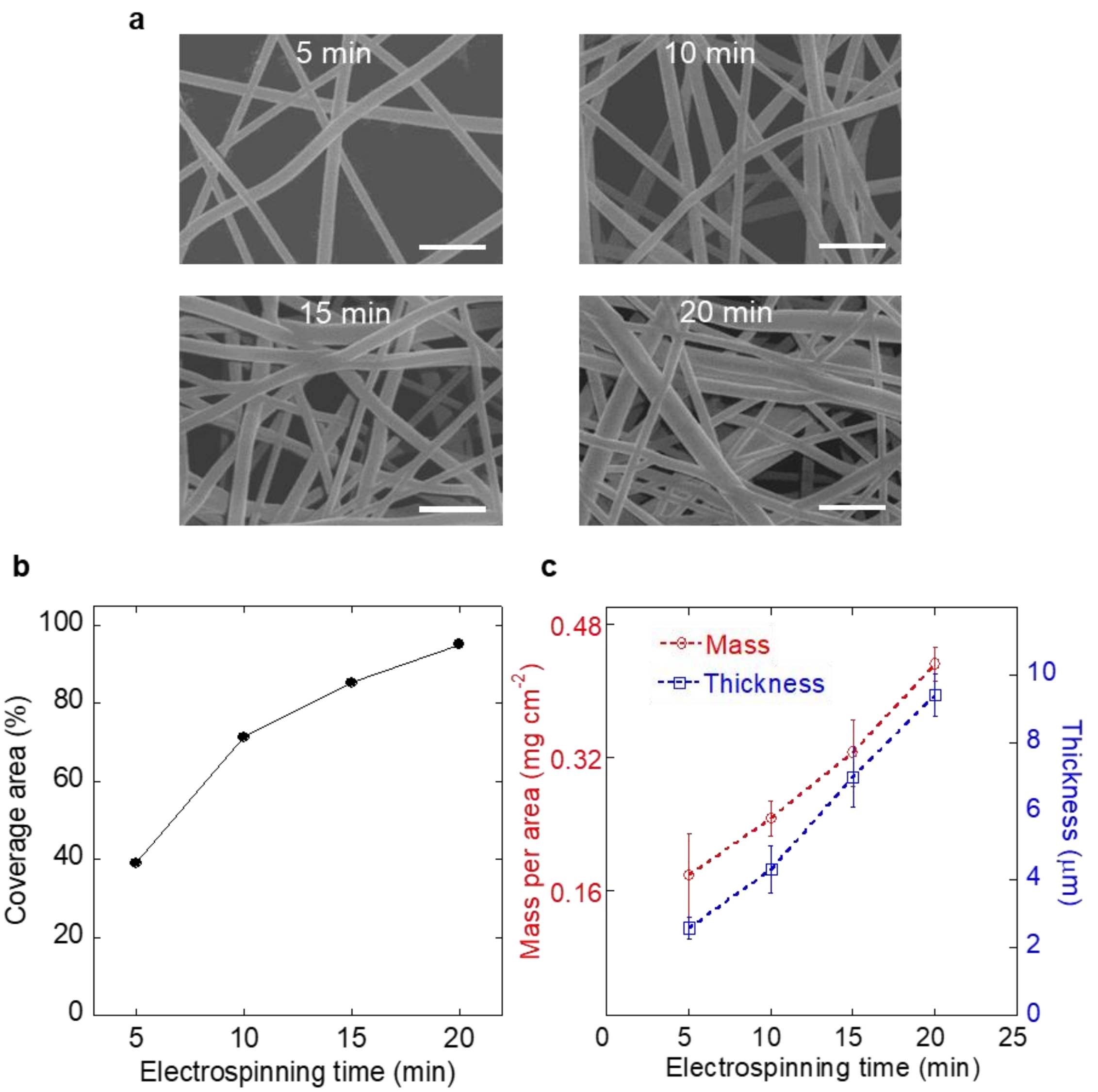

Figure S6

Light-weight feature of all-nanofiber sensor. a, SEM image of nanofiber substrates at different electrospinning time. Scale bar, 5 µm. **b,** Maximum coverage area (percentage) as a function of electrospinning time. **c,** Mass and thickness of nanofiber substrate as function of electrospinning time (n = 3). Red curve represents mass and blue represents thickness.

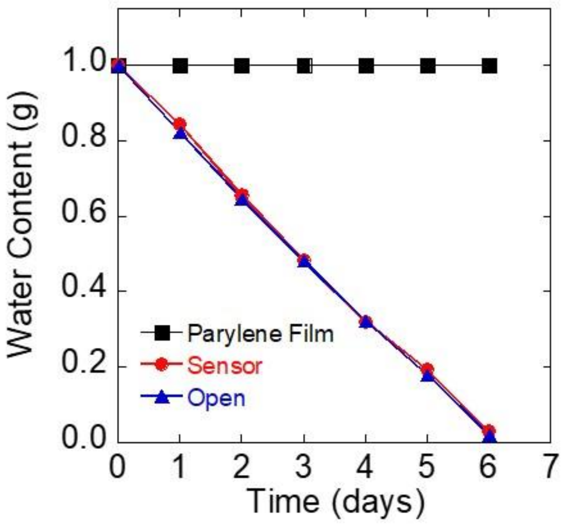

Figure S7

Gas-permeability of all-nanofiber mechanoacoustic sensor.

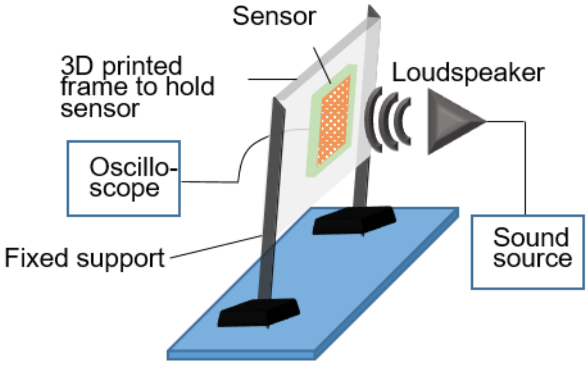

Figure S8

Experimental setup for the characterization of all-nanofiber mechano-acoustic sensor.

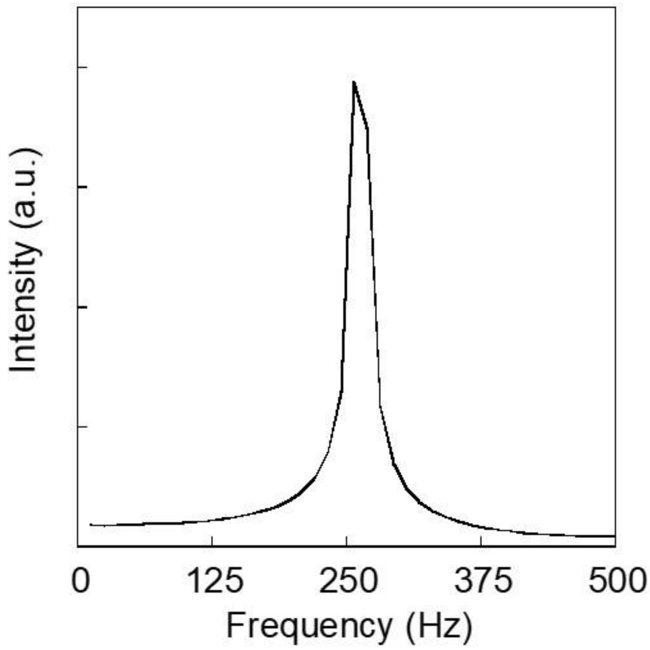

Figure S9

FFT pattern of generated voltage signal when sound waves of 250 Hz at 110 dB is applied to sensor.

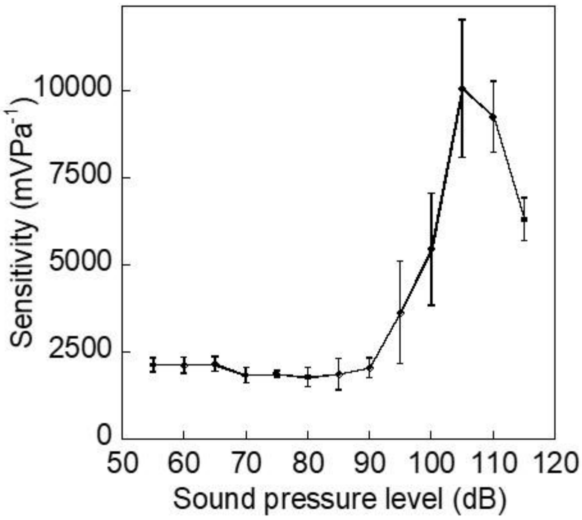

Figure S10

Sensitivity of all-nanofiber mechano-acoustic sensor over a wide range of sound pressure level (SPL) (n = 3).

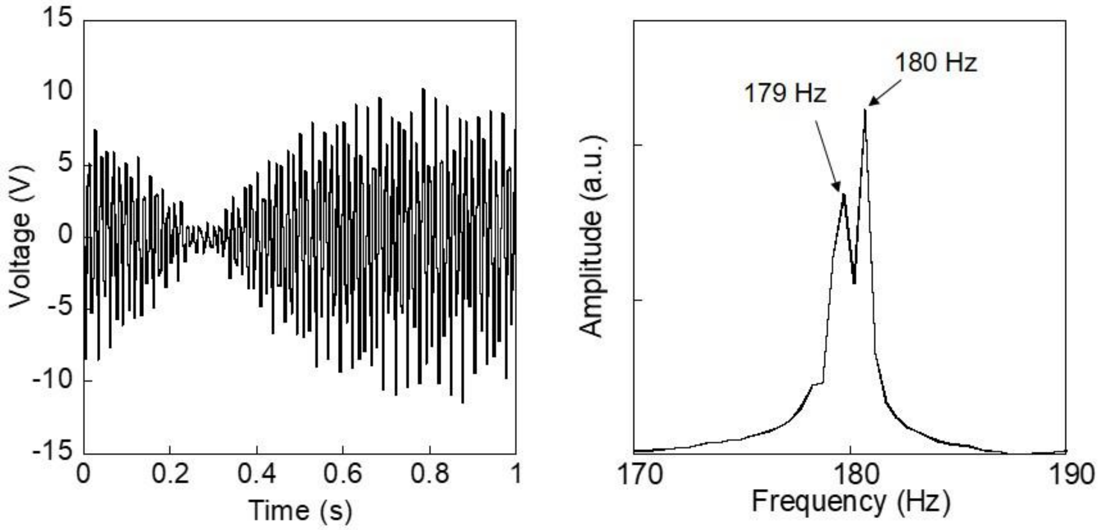

Figure S11

Voltage waveform when two signals with closer frequency (179 and 180 Hz) are applied to sensor (left) and corresponding FFT pattern (right). Sensors can differentiate two signals of 1 Hz gap showing very high resolution of frequency differentiation.

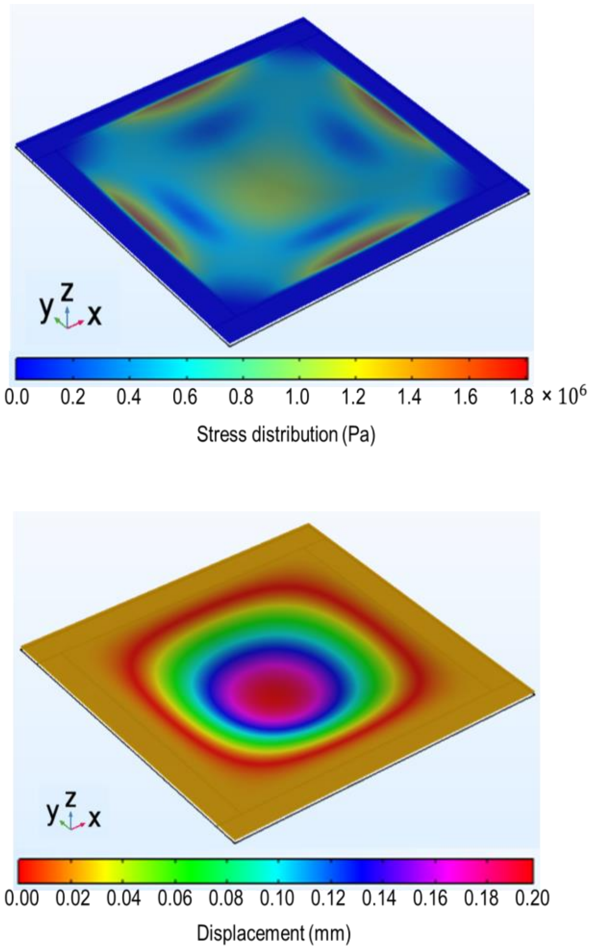

Figure S12

Simulation of device vibration when sound waves of fixed frequency and SPL is applied (COMSOL Multiphysics 3.5a). Distribution of stress (top) and total displacement (bottom) of devices due to the application of sound waves at 250 Hz. Each nanofiber layer is considered as low density film layer. The parameters used for PVDF layer and substrate layers are as follows; PVDF: density = 450 Kg m^{-3}, Poisson's ratio = 0.42 and Young's modulus = 1.5 GPa; Substrates: density = 1420

Kg m^{-3}, Poisson's ratio = 0.34 and Young's modulus = 2.5 GPa. The sound source is considered as a point source located 1 cm away from the sensor.

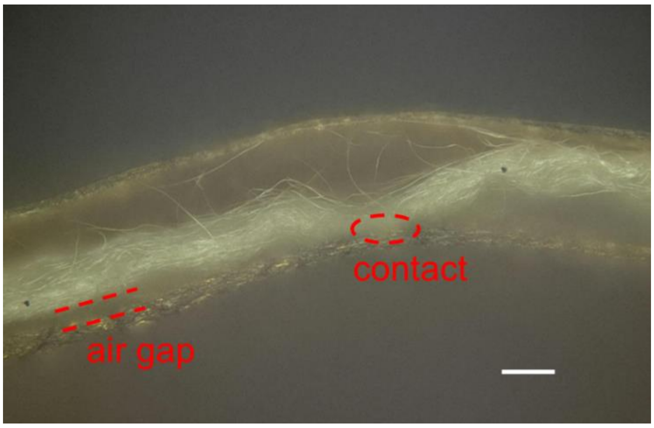

Figure S13

Microscopic cross-section of all-nanofiber mechano-acoustic sensors. Scale bar, 10 μm.

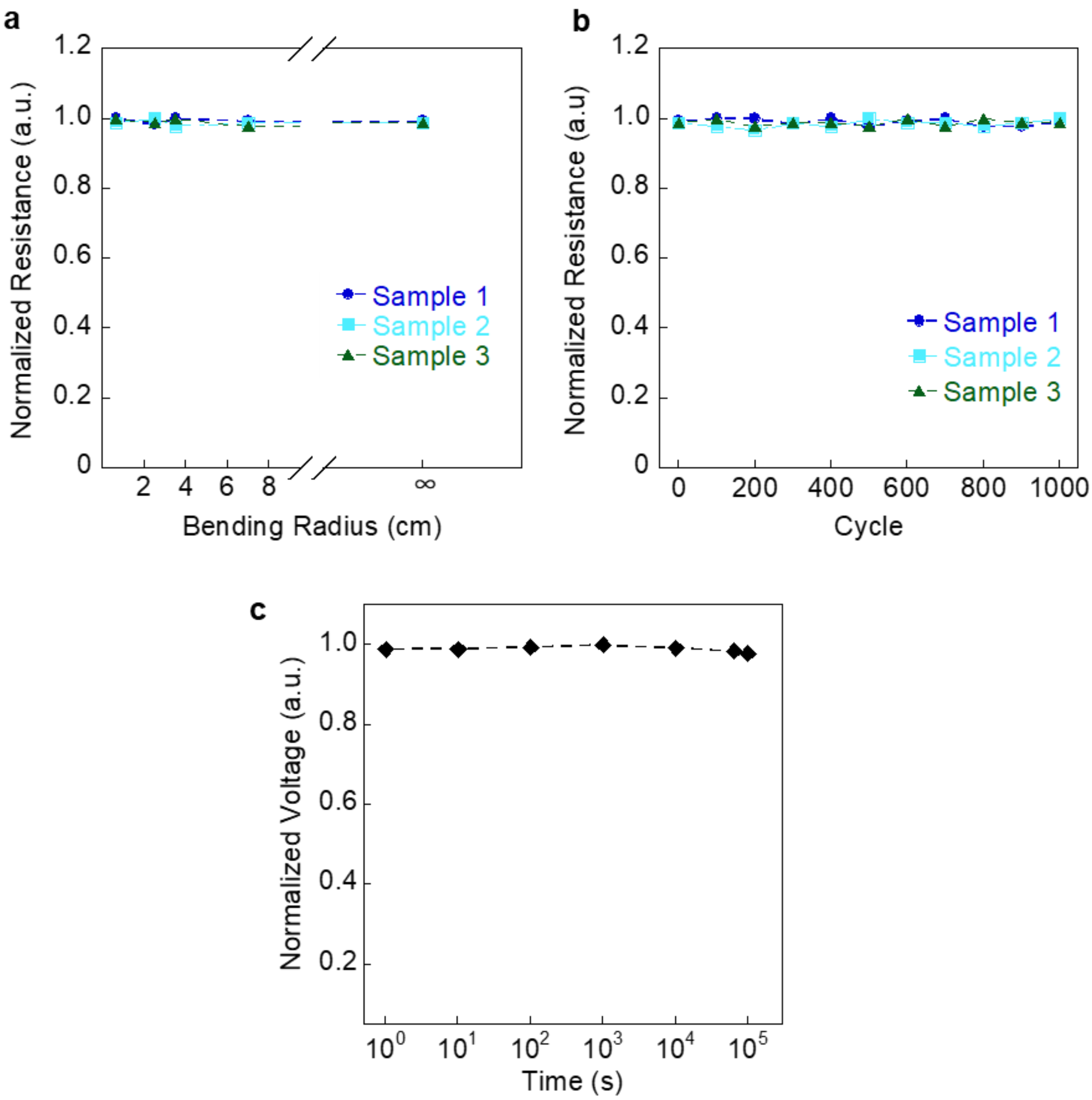

108

109 **Figure S14**

110 **a**, Normalized resistance at different bending radii, ranging from the flat state (∞) to a 6.5
111 mm bending radius. **b**, Cyclic durability of up to 1000 repetitive bending cycles (bending
112 radius, 6.5 mm). **c**, Long-term stability of sensor when a sound wave (250 Hz and 110
113 dB) is applied continuously for 27 h.

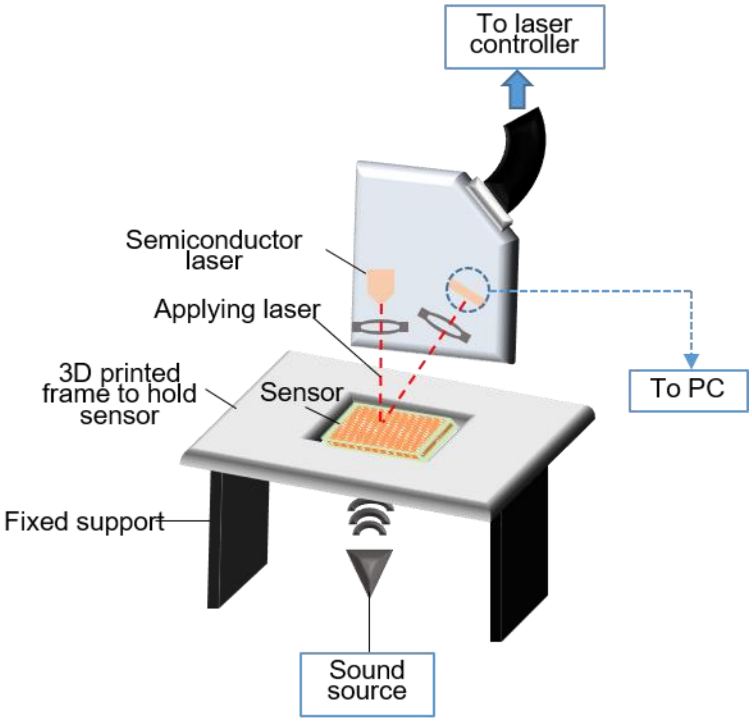

Figure S15

Experimental setup for the measurement of vibration amplitude of sensors.

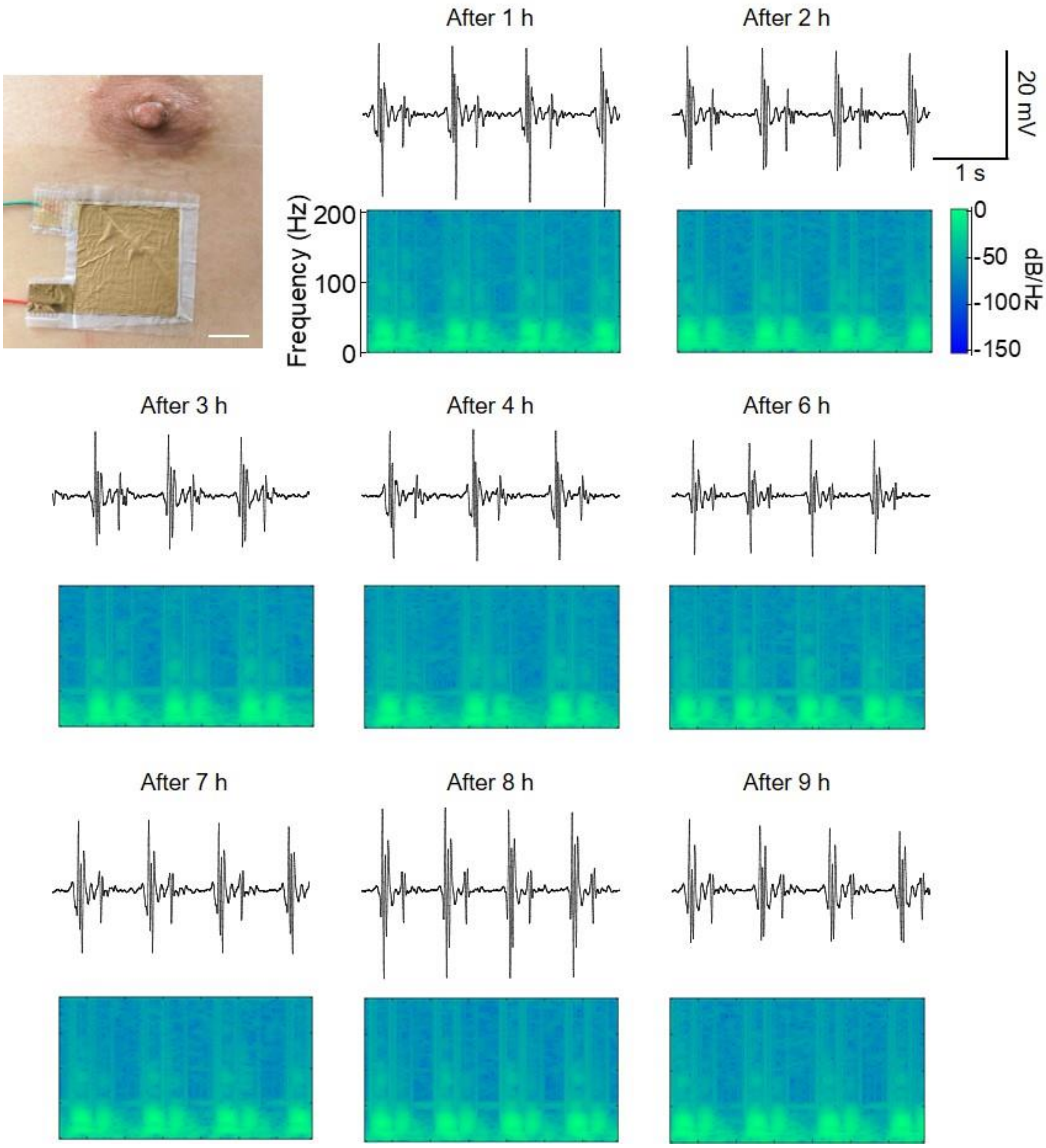

Figure S16

Optical photo of sensor attached at the mitral valve position of human chest for long-term seismocardiography. Scale bar, 1 cm. Mechano-acoustic heart signals (after 1 h, after 2 h, after 3 h, after 4 h, after 6 h, after 7 h, after 8 h and after 9 h), and the corresponding spectrograms.

Table S1. A comparison of water-vapor permeability of nanofiber-based devices

References	Water-vapor permeability ($Kg\ m^{-2}\ d^{-1}$)
Y. Li, F. Yang, J. Yu, B. Ding, Hydrophobic Fibrous Membranes with Tunable Porous Structure for Equilibrium of Breathable and Waterproof Performance. Adv. Mater. Interfaces **3**, 1600516 (2016).	11.9
J. Sheng, M. Zhang, Y. Xu, J. Yu, B. Ding, Tailoring Water-Resistant and Breathable Performance of Polyacrylonitrile Nanofibrous Membranes Modified by Polydimethylsiloxane. ACS Appl. Mater. Interfaces **8**, 27218–27226 (2016).	12.5
F. Yang, et al., Hydrophobic polyvinylidene fluoride fibrous membranes with simultaneously water/windproof and breathable performance. RSC Adv. **6**, 87820–87827 (2016).	11.5
Z. Li, et al., All-Fiber Structured Electronic Skin with High Elasticity and Breathability. Adv. Funct. Mater. **30**, 1908411, 1–9 (2019).	10.3
A. Miyamoto, et al., Inflammation-free, gas-permeable, lightweight, stretchable on-skin electronics with nanomeshes. Nat. Nanotechnol. **12**, 907–913 (2017).	10.7
This work	**12.4**

List of Supplementary Movies

Movie S1

Observation of the real-time vibration and the contact-separation between the layers of the sensor using high-speed camera under the application of sound waves (100 Hz) (normal speed).

Movie S2

Observation of the real-time vibration and the contact-separation between the layers of the sensor using high-speed camera under the application of sound waves (100 Hz) (10x slower speed).

References

1. G. Fan, et al., Hierarchical porous carbon nanofibrous membranes with an enhanced shape memory property for effective adsorption of proteins. RSC Adv. **5**, 64318–64325 (2015).
2. S. J. Park, et al., Surface Engineering of Triboelectric Nanogenerator with an Electrodeposited Gold Nanoflower Structure. Sci. Rep. **5**, 13866 (2015).